Molecular Genetics and Metabolism 143 (2024) 108537

Contents lists available at ScienceDirect

Molecular Genetics and Metabolism

journal homepage: www.elsevier.com/locate/ymgme

Reduction of neuroinflammation and seizures in a mouse model of CLN1 batten disease using the small molecule enzyme mimetic, N-Tert-butyl hydroxylamine

Zach Fyke [a], Rachel Johansson [f,g], Anna I. Scott [g,i], Devin Wiley [g], Daniel Chelsky [g], Joseph D. Zak [d,e], Nader Al Nakouzi [g,**], Kevin P. Koster [a,h,*], Akira Yoshii [a,b,c]

[a] Department of Anatomy and Cell Biology, University of Illinois at Chicago, Chicago, IL, United States of America
[b] Department of Pediatrics, University of Illinois at Chicago, Chicago, IL, United States of America
[c] Department of Neurology, University of Illinois at Chicago, Chicago, IL, United States of America
[d] Department of Biological Sciences, University of Illinois at Chicago, Chicago, IL, United States of America
[e] Department of Psychology University of Illinois at Chicago, Chicago, IL, United States of America
[f] School of Medicine, University of California Davis, Sacramento, CA, United States of America
[g] Circumvent Pharmaceuticals, Portland, OR, United States of America
[h] Department of Neurobiology, University of Chicago, Chicago, IL, United States of America
[i] Department of Laboratories, Seattle Children's Hospital, Seattle, WA, United States of America

ARTICLE INFO

Keywords:
Infantile neuronal ceroid lipofuscinosis
Neurodegeneration
Palmitoyl-protein thioesterase
Neuroinflammation
Seizure
Synapse calcium
Batten disease
Small molecule therapeutic

ABSTRACT

Infantile neuronal ceroid lipofuscinosis (CLN1 Batten Disease) is a devastating pediatric lysosomal storage disease caused by pathogenic variants in the *CLN1* gene, which encodes the depalmitoylation enzyme, palmitoyl-protein thioesterase 1 (PPT1). CLN1 patients present with visual deterioration, psychomotor dysfunction, and recurrent seizures until neurodegeneration results in death, typically before fifteen years of age. Histopathological features of CLN1 include aggregation of lysosomal autofluorescent storage material (AFSM), as well as profound gliosis. The current management of CLN1 is relegated to palliative care. Here, we examine the therapeutic potential of a small molecule PPT1 mimetic, N-tert-butyl hydroxylamine (NtBuHA), in a *Cln1*$^{-/-}$ mouse model. Treatment with NtBuHA reduced AFSM accumulation both in vitro and in vivo. Importantly, NtBuHA treatment in *Cln1*$^{-/-}$ mice reduced neuroinflammation, mitigated epileptic episodes, and normalized motor function. Live cell imaging of *Cln1*$^{-/-}$ primary cortical neurons treated with NtBuHA partially rescued aberrant synaptic calcium dynamics, suggesting a potential mechanism contributing to the therapeutic effects of NtBuHA in vivo. Taken together, our findings provide supporting evidence for NtBuHA as a potential treatment for CLN1 Batten Disease.

1. Introduction

The neuronal ceroid lipofuscinoses (NCLs), historically identified as Batten Disease, represent a spectrum of autosomal recessively inherited neurodegenerative diseases caused by pathogenic changes in one of 14 genes identified to date [1–3]. Infantile NCL (aka CLN1, Batten Disease type 1) is a particularly devastating subtype [3]. Symptom onset in CLN1 typically presents around six months of age with progressive blindness, psychomotor dysfunction, and recurrent seizures, ultimately culminating in fatality by 15 years of age [4–10].

Seizures in patients with CLN1 may present before a diagnosis is made and are often present very early in the disease course [8]. Seizures can be as frequent as multiple times a day with types varying from focal to primary generalized seizures [8]. Seizures in CLN1 Batten Disease are often debilitating for patients and challenging for caregivers. Current management of seizures include existing anti-seizure medications with varying efficacy. Depending on seizure type, duration, and age of onset, the neurocognitive effects can range from synaptic-circuit reorganization to neuronal cell death [11]. More effective seizure control earlier in the disease course might improve quality of life for patients and

* Correspondence to: Kevin P. Koster, University of Chicago, 947 East 58th Street, MC 0928, Chicago, IL 60637, United States of America.
** Correspondence to: Nader Al Nakouzi, Circumvent Pharmaceuticals, 71 N Wilson Ave. Unit 4, Pasadena, CA 91106-2320, United States of America.
E-mail addresses: naderalnakouzi@gmail.com (N. Al Nakouzi), kpkoster@uchicago.edu (K.P. Koster).

https://doi.org/10.1016/j.ymgme.2024.108537
Received 30 April 2024; Received in revised form 11 June 2024; Accepted 12 July 2024
Available online 15 July 2024

caregivers, as well as reduce the long-term harmful effects of repeated seizures on neuronal function.

CLN1 is caused by pathogenic variants of the depalmitoylation enzyme, palmitoyl-protein thioesterase 1 (PPT1). Protein palmitoylation (S-acylation) is a reversible post-translational modification linking palmitate, a 16-carbon fatty acid, to proteins [12]. Palmitoylation dynamics influence multiple cellular functions and are critical for regulating protein trafficking and degradation [12–14]. Palmitoylation is orchestrated by more than twenty palmitoyl acyltransferases (PATs), frequently localized to the Golgi apparatus, where they catalyze covalent bonding of palmitate to target proteins [15,16]. Depalmitoylation is carried out by only a few enzymes, including PPT1, which localizes to several cellular compartments but chiefly the lysosome [14,17,18]. Accordingly, autofluorescent storage material (AFSM) consists of accumulated palmitoylated proteins in lysosomes and is a histopathological hallmark of CLN1. AFSM is a shared microscopic finding of NCLs and was described before the identification of disease-causing genes [3,6,7].

Among all the NCLs, there is currently only one clinically approved, disease-modifying treatment that is exclusive to CLN2 [19]. For CLN1, disease-modifying therapeutics are not commercially available. Current treatments focus on symptom management and palliative care measures [8]. While gene and enzyme replacement therapies successfully mitigate disease symptomology in CLN1 mouse models [20–24], enthusiasm for elevating these therapies to human clinical trials hinges on optimizing their delivery and expression, as well as their safety profile [25]. An adjunctive strategy to treat CLN1 is small molecule therapeutics, particularly those that mimic the endogenous function of PPT1. In previous work, Sarkar and colleagues (2013) demonstrated that the hydroxylamine derivative N-tert-butyl hydroxylamine (NtBuHA) can cleave the thioester linkage of post-translational palmitoyl modifications, effectively acting as a depalmitoylase capable of counteracting the loss of PPT1 function. Indeed, NtBuHA administration reduced histopathological markers of CLN1, improved motor function, and increased lifespan in *Cln1*$^{-/-}$ mice [26]. However, poor stability of the previous salt form under standard storage conditions renders it impractical for future use in human patients.

Here, we tested the therapeutic efficacy of PPT1-mimetic supplementation in *Cln1*$^{-/-}$ mice [27] using a novel citrate salt formulation of NtBuHA called CIRC827 that significantly improves its stability under ambient conditions. We discovered that this new form of NtBuHA reduced AFSM accumulation both in vitro and in vivo, improved primary neuronal calcium dynamics, attenuated neuroinflammation, mitigated seizures, and rescued motor function in *Cln1*$^{-/-}$ mice. These results confirm that small molecule PPT1-mimetic treatment is a potential therapeutic approach for CLN1 and provides novel mechanistic insight into its beneficial effects.

2. Materials and methods

2.1. Animals, genotyping, group allocation, and data handling

Animal procedures, genotyping, and data handling were performed as previously [28,29]. *Cln1*$^{+/-}$ (heterozygous) mice were obtained from Jackson Laboratory and maintained on 12 h light/dark cycle with food and water ad libitum. Animals were genotyped in-house as first demonstrated [27] and used for experiments at specified multiple disease-relevant time points: postnatal day 60 (P60) and P180. Data were either analyzed by lab members blinded to condition or randomized prior to analysis by ZAF and JDZ. All animal procedures were performed in accordance with the guidelines of the University of Illinois of Chicago Institutional Animal Care and Use Committee (Protocol# 21–075).

2.2. NtBuHA drug solubilization and administration

NtBuHA (Circumvent Pharmaceuticals, see *Key Resources Table*) was received as 40-g aliquots in amber glass jars wrapped in parafilm and kept at room temperature out of direct sunlight. Since NtBuHA is hydrophilic, the compound was solubilized via serial dilutions ranging from 0.1 μM to 1 mM NtBuHA in PBS pH 7.4 for the treatment of primary cortical neuron culture. For ad libitum dosing to wild-type (WT) and *Cln1*$^{-/-}$ animals, NtBuHA was prepared in standard animal care facility water bottles at a concentration of 250 μM, 1 mM, and 4 mM. Fresh drug aliquots were administered by lab members weekly, with animals' weights monitored from P30–60 for potential side effects of drug treatment. First, a pilot study was performed to monitor potential adverse reactions to drug treatment across the three aforementioned doses, in which no adverse effects were observed at any dose. Next, a short-term treatment was performed from P30-P60 using a dose of 1 mM, to match the dosage used by a previous study (Sarkar et al., 2013). For chronic (6 month) dose selection, results from a good laboratory practices (GLP) compliant toxicology study were considered (FDA and OECD compliant study results provided by Circumvent Pharmaceuticals and performed at Charles River Laboratories; data not shown), which revealed that daily oral administration of 100 mg/kg is well within the NOAEL (no observed adverse effect level) for NtBuHA and is closer to the prospective dosing in humans. This daily dose corresponds to the amount consumed in drinking water containing 4 mM NtBuHA. Therefore, 4 mM NtBuHA dosing was selected for long-term experiments (6-month histology, EEG, and rotarod testing) to enhance the clinical relevance of our treatment paradigm.

Resources Table Mouse Strains

B6;129-Ppt1tm1Hof/J	Jax stock #: 004313	RRID: MGI:004313

Antibodies		
Reagent or Resource	Source	Identifier
Paraformaldehyde	Thermo Scientific Chemicals	Cat# AA47377-9 M
Superfrost Plus Microscope Slides	Fisher Scientific	Cat# 12–550-15
Anti MAP2, Rabbit	Millipore-Sigma	RRID: AB_5622
Alexa Fluor 633 Goat anti-Rabbit	Invitrogen Antibodies	RRID: AB_2535731
Anti GFAP, Goat	Abcam	RRID: AB_53554
Alexa Fluor 488 Donkey Anti-Goat IgG	Jackson ImmunoResearch Laboratories	RRID: AB_2336933
Anti Iba1, Rabbit	Fujifilm	Code No. 019–19,741
Vectashield Plus Antifade Mounting Medium with DAPI	Vector Laboratories	SKU# H-1200-10
Donkey Serum	Sigma-Aldrich	Cat# D9663-10ML

Reagents, Chemicals, and Recombinant DNA		
N-tert-butyl-hydroxylamine	Circumvent Pharmaceuticals	N/A
Hank's Balanced Salt Solution (HBSS)	Gibco	Cat# 14170112
Papain	Worthington Biochemical	Cat# 9001-73-4
DNase I	Millipore-Sigma	Cat# 69182-1000UN
B27 Plus Neuronal Culture System	Gibco	Cat# A3653401
35 mm Glass Bottom Culture Dish	Cellvis	Cat# NC0794151
Poly-D lysine hydrobromide	Millipore-Sigma	Cat# P7886-10MG
Mouse Laminin	Corning	Cat# 354232
Maxi Plasmid Purification Kit	Invitrogen	Cat# A31217
CAG-GCaMP3	Addgene	Cat# 22692
Lipofectamine 2000	Invitrogen	Cat# 11668019

(*continued on next page*)

(*continued*)

Reagents, Chemicals, and Recombinant DNA		
N-tert-butyl-hydroxylamine	Circumvent Pharmaceuticals	N/A

Implants & Tools		
DSI ETA F-10 Mouse Implantable Transmitter	Data Sciences International	N/A
DSI RPC-1 Receiver	Data Sciences International	N/A
DSI Data Exchange Matrix (MX1)	Data Sciences International	N/A
Actril Cold Sterilant	VWR	Cat# W2T886023
Temporary Crown & Bride Material (A1)	Defend by Mydent International	REF: CB-9000

Software & Algorithms		
Ponema Version 5.2	Data Sciences International	N/A
Neuroscore Version 3.1	Data Sciences International	N/A
Prism 9	GraphPad	RRID: SCR_002798
FIJI Version 2.9.0	Fiji/ImageJ	RRID: SCR_002285
Biorender	Biorender	RRID: SCR_018361
CaImAn	Flatiron Institute	N/A
MATLAB	MathWorks	RRID:SCR_001622

2.3. Primary cortical neuron culture and transfection

Primary cortical neuron culture was conducted as described previously [28,29]. Briefly, timed pregnancies from *Cln1*$^{-/+}$ dams were grown until embryonic day 15.5 (E15.5). For live-cell imaging experiments, cells were counted and then plated at 350,000–400,000 cells/dish on 35 mm cell culture dishes containing poly-D-lysine/laminin-coated coverslips (Cellvis). Cells were grown until DIV7 (day in vitro), and then were transfected as described in Koster et al. [28,29]. In summary, $GCaMP_3$ (4 μg DNA/dish) was combined in a transfection construct containing both Lipofectamine 2000 (2 μg/dish) and Neurobasal plus B27 neuronal culture media. Transfection solution was applied to the primary neurons which were incubated at 37 °C for 45 min. Neurons recovered until DIV14, at which point *Cln1*$^{-/-}$ samples were treated with 100 μM NtBuHA every 48 h from DIV12–18. (See *Key Resources Table*).

2.4. Immunocytochemistry and microscopy imaging and analysis

For immunocytochemistry (ICC) experiments, primary neurons were dissociated, cells were counted then plated at 150,000–180,000 cells/well in 24-well plates containing poly-D-lysine/laminin-coated coverslips. ICC neuronal culture was grown until DIV7, then treatment was administered via a 1:1000 dilution of NtBuHA at indicated concentrations every 48 h until DIV18. Finally, cells were fixed in 4% paraformaldehyde (PFA) solution. Immunostaining was performed as described previously [29]. In short, neurons were stained for microtubule-associated protein 2 (Anti-MAP2, Rabbit; Millipore-Sigma; RRID: AB_5622). Following primary antibody incubation, coverslips were then incubated in the fluorophore-linked secondary antibody (Alexa Fluor 633 Goat anti-Rabbit; Invitrogen Antibodies; RRID: AB_2535731). Coverslips were mounted on SuperFrost Plus slides in DAPI Vectamount medium. To investigate AFSM accumulation after NtBuHA treatment, primary neurons were grown until DIV7, then treated with 1:1000 dilutions of either vehicle (PBS) or 0.1–1.0 mM NtBuHA every 48 h until DIV19. After the final treatment, cells were washed in PBS before fixation in 4% PFA in PBS.

For in vitro AFSM particle detection, confocal imaging was performed using the LSM710 confocal microscope with Zen Black imaging software. *Z*-stack max projection images of monolayer primary neurons (for a total of 10 μm of z-plane depth to properly encompass the entirety of the cell's soma) were collected. Next, the open-source image analysis software FIJI was used to create max-projection compressions of all imaging channels including DAPI (405 nm), AFSM (555 nm), and MAP2 (633 nm). Next, image channels were separated, a single neuron was selected, and the cell soma was encircled as a region of interest (ROI). Then, the corresponding nucleus was cleared across channels to isolate somatic fractions containing AFSM. The default threshold algorithm was used to generate a binary mask of AFSM puncta. The number of puncta, total area, and percent area were derived using the 'analyze particles' tool (>2^2 pixels). These data were then input to Prism Graph Pad 9 for graphs and statistics. (See *Key Resources Table*).

2.5. Transcardial perfusion and immunohistochemistry

Transcardial perfusion, immunohistochemistry, and image analysis were performed as described previously [28,29]. Briefly, untreated and NtBuHA treated *Cln1*$^{-/-}$ and WT mice were anesthetized with isoflurane and transcardially perfused with PBS followed by 4% PFA in PBS. Brains were removed and fixed overnight at 4 °C in PFA, then transferred to 30% sucrose in PBS before sectioning. 100 μm coronal sections were made in cold PBS using a Vibratome 1000 (Technical Products International, St. Louis, MO). Four serial sections per well were stored in a cryoprotectant solution (30% glycerol, 30% ethylene glycol in PBS) at −20 °C until immunohistochemistry was performed. Three to four brain slices per animal were isolated from primary somatosensory cortex (S1) and primary visual cortex (V1) and were first incubated in PBS before undergoing permeabilization. Next, samples underwent antigen retrieval by heating in Tris-EDTA. Brain sections were blocked (TBS + 0.1% Triton X-100, 4% BSA, and 5% normal goat serum) before incubating in rabbit anti-Iba1 (Anti Iba1, Rabbit; Fujifilm; Code No. 019–19,741) for 48 h. After 4 PBS washes of 10 min each, tissue was incubated in Alexa Fluor 633 (Goat anti-Rabbit; Invitrogen Antibodies; RRID: AB_2535731). After washing, the tissue was incubated in GFAP antibody (Anti-GFAP, Goat; Abcam; RRID: AB_53554) for 48 h. Then, the slices were incubated in Alexa Fluor 488 (Donkey Anti-Goat IgG; Jackson ImmunoResearch Laboratories; RRID: AB_2336933). Finally, two slices from S1 and two slices from V1 were mounted on SuperFrost Plus slides in DAPI Vectamount medium. (See *Key Resources Table*).

2.6. In vivo histology analysis

Two z-stack images from L2/3 of S1 and V1 from each animal were acquired using a Zeiss LSM710 confocal laser scanning microscope at 63× magnification. All sections were imaged using identical parameters. Quantification of AFSM was performed by creating a max projection z-stack compression (20 μm/ 1 image per micron) and subsequent background subtraction and automated images thresholding in FIJI (See *Key Resources Table*), generating an 8-bit binary mask of AFSM-positive pixels (>5 pixels^2). The identical threshold was applied to each image (Default threshold algorithm). The number of AFSM particles above threshold, as well as percent area occupied by AFSM puncta, the average puncta size, and total AFSM area was then calculated using the "analyze particles" tool. GFAP histology was performed as described for AFSM particles, with the threshold for astrocyte arbors set at >15 pixels^2. Individual GFAP astrocyte counts were made by an analyst, blinded to treatment condition, and were described as a fully stained cell body along with four directly connected processes. IBA1 microglial Scholl analysis was completed as previously described [29]. Briefly, 20 μm z-stack compressions were made in the 633 nm confocal imaging channel. Three microglia per image, five images from S1 and five images from V1 were isolated and thresholded using the 'default' algorithm. An ROI was set in the center of the cell soma, to which we applied the neuroanatomy plug-in 'skeletonize' to trace microglial ramifications. Next, we used the

Scholl Analysis plug-in, setting the concentric ring distance at 2 μm step size, with the first concentric ring starting at 5 μm from the cell soma and expanding to 70 μm. The number of microglial ramifications that intersect with each ring was graphed, with the corresponding distance from the cell soma indicated. For all IHC experiments, three animals per condition were used for analysis.

2.7. Live cell imaging

Live cell imaging was performed as previously described [29]. At DIV8, primary cortical neuron cultures from WT and *Cln1*$^{-/-}$ cultures were transfected to express $GCaMP_3$ as described above. Then, cultures were maintained until DIV12 where each dish received either vehicle (PBS) or 100 μM NtBuHA via 1:1000 dilution into cell culture media. Treatment was administered once on DIV12 and again on DIV14, two hours prior to live cell imaging. Next, 4-min videos of a single transfected neuron were taken at 10× magnification using the LSM 710 confocal microscope at a rate of 4 frames/ s.

2.8. Calcium imaging analysis

Images were exported as raw TIFF files for processing using custom and available MATLAB scripts. Prior to processing, images were binned at 2 × 2 by averaging pixel values in each bin. Non-rigid motion artifact compensation and denoising were then performed using NoRMcorre [30]. The CaImAn CNMF pipeline [31] was used for ROI selection (See *Key Resources Table*). ROIs were further filtered by size and shape to remove merged cells. The analysis pipeline was optimized for in vitro imaging [32] and for the selection of subcellular structures [33]. Calcium transients were identified by local maxima and included if the peak amplitude exceeded 3.5 standard deviations of a noise distribution obtained from baseline samples. Instantaneous event frequencies were calculated by considering the rate of spontaneous calcium events across all synaptic sites associated with a single neuron and interleaving event timestamps.

2.9. EEG transmitter implantation & data acquisition

EEG transmitter implantation was performed as recently described [34]. Briefly, 6.5-month-old WT and *Cln1*$^{-/-}$ animals were anesthetized using 1.5–3% isoflurane and then head-fixed in the stereotaxic apparatus. Hair was removed from the scalp of the animal, and the skin was sterilized with ethanol wipes and iodine swabs. A 1.5 to 2 cm incision was made along the midline of the skull just anterior to bregma to the rostral border of the trapezius muscles. Then, an ETA-F10 wireless radiotelemetric transmitter weighing 1.6 g (ETA-F10, Data Sciences International, St. Paul, MN) was inserted into a subcutaneous pocket, made using blunt scissors above the left hindlimb. Two biopotential leads were fixed unilaterally and subdurally above the motor cortex (M1) and visual cortex (V1) by screws. Each lead was wrapped securely around a single screw. The leads and screws were secured by covering with dental cement (See *Key Resources Table*). Once the cement was dry, the incision was closed using 4–0 monofilament suture with a simple interrupted pattern. After the suture was completed, antibiotic ointment was liberally applied to the incision prior to the animal's recovery on a heating pad.

2.10. Telemetric recording of unilateral EEG activity

After recovery from surgery, mice were moved to recording cages to acclimatize. At the time of recording, telemetric transmitters were magnetically activated. EEG data was collected as described previously [35]. The cages were mounted on a DSI telemetry receiver (RPC-1), connected to a DSI Data Exchange Matrix (MX1) and subsequently to an acquisition computer. EEG recordings were conducted 24–36 h post-implantation using Ponema (Ver 5.20). Once 24-h EEG recordings were complete, telemetry units were inactivated, and animals were euthanized at 72 h.

2.11. EEG data processing and analysis

EEG traces were uploaded as .RAW files and imported into DSI's analysis software (Neuroscore Ver 3.1). For data analysis, the dynamic spike detection threshold was manually configured to identify epileptiform spikes >5× above baseline EEG signal. The spike detection algorithm was used to generate seizure reports for each animal by an experimenter, blinded to the treatment condition. Data were generated and analyzed as described [34], using a manual analysis paradigm. A subset of EEG recordings included video corresponding to time-stamped EEG traces for a quantitative confirmation of severe convulsive epileptic episodes from both untreated and NtBuHA-treated *Cln1*$^{-/-}$ mice (Supplementary Video 1–2). Prism Graph Pad 9 and Biorender were used to generate graphs and statistics and illustrations.

2.12. Rotarod testing

Single-speed rotarod testing was completed in WT and *Cln1*$^{-/-}$ mice at 2 months, 4 months, and 6months of age. For each test, animals were acclimatized to the testing room for one hour prior to training. Next, animals were placed on an ENV-577 with the speed set to 16 RPM for 1 min. Two training trials of one minute were completed, with a minimum of 10 min break between training rounds. After training was complete, the animals were placed on the rotarod at 16 RPM for 3 min, with the latency to fall recorded by an experimenter, blinded to treatment condition. At the cessation of the trial, three testing round scores were averaged to generate the average latency to fall. Prism Graph Pad 9 was used to generate graphs and statistics.

3. Results

3.1. NtBuHA administration reduces AFSM in *Cln1*$^{-/-}$ primary cortical mouse neurons

First, we tested whether NtBuHA could reduce the aggregation of AFSM in primary cortical neurons derived from embryonic *Cln1*$^{-/-}$ mice. Wild-type (WT) and *Cln1*$^{-/-}$ mouse primary neurons were treated with either vehicle (PBS) or NtBuHA every 48 h for 12 days (Supplemental Fig. 1 A, 1B). Following the final treatment, neurons were fixed, immunostained for MAP2 and analyzed for AFSM accumulation (Fig. 1A). Automated particle analysis of AFSM in neuronal soma showed that, as expected, WT neurons did not accumulate AFSM, while untreated *Cln1*$^{-/-}$ primary neurons typically contained multiple AFSM puncta (Fig. 1A). Importantly, after treatment with NtBuHA, we observed a dose-dependent reduction in the number of AFSM puncta compared to untreated *Cln1*$^{-/-}$ neurons (Fig. 1B). Similarly, the percent area of AFSM deposits within the soma of NtBuHA-treated *Cln1*$^{-/-}$ primary neurons (Fig. 1C) and size of puncta (Supplemental Fig. 1C) were also reduced.

3.2. Treatment with NtBuHA reduces AFSM accumulation and attenuates neuroinflammation in *Cln1*$^{-/-}$ mice

To validate and extend our in vitro findings, we tested the effect of early therapeutic supplementation of NtBuHA in *Cln1*$^{-/-}$ mice. We initially performed a short-term treatment paradigm at the dosage utilized by Sarkar and colleagues (2013), 1 mM. Beginning at postnatal day 30 (P30), *Cln1*$^{-/-}$ mice were given free access to either drinking water or water supplemented with NtBuHA. We then analyzed AFSM accumulation in the primary somatosensory (S1) and visual cortices (V1) of treated and untreated *Cln1*$^{-/-}$ animals at 2 months (P60) (Fig. 2A-C). As demonstrated previously [28], AFSM accumulation in *Cln1*$^{-/-}$ animals was modest by P60 (Fig. 2A). Both the AFSM puncta count (Fig. 2B) and

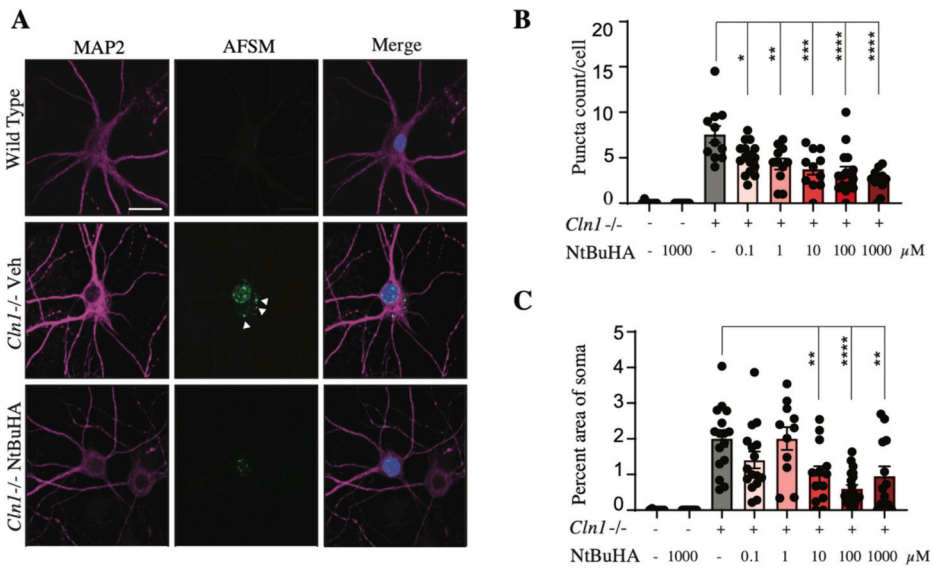

Fig. 1. NtBuHA Reduces AFSM Accumulation in *Cln1*$^{-/-}$ Neuron Culture. (A) Representative images of WT, *Cln1*$^{-/-}$, and NtBuHA-treated *Cln1*$^{-/-}$ neurons immunostained for MAP2 and DAPI and demonstrate the presence of AFSM deposits in neuronal somata (arrowheads). Scale = 25 μm. (B) Quantification of AFSM puncta count per cell, *Cln1*$^{-/-}$ vehicle-treated = 7.488 particles, $n = 29$ cells/3 embryos; comparison to *Cln1*$^{-/-}$ 0.1 μM NtBuHA = 5.157 particles, $n = 28$ cells/3 embryos, $P = 0.0358$; comparison to *Cln1*$^{-/-}$ 1 μM NtBuHA = 4.511 particles, $n = 25$ cells/3 embryos, $P = 0.0042$; comparison to *Cln1*$^{-/-}$ 10 μM NtBuHA = 4.071 particles, n = 25 cells/3 embryos, $P = 0.0002$; comparison to *Cln1*$^{-/-}$ 100 μM NtBuHA = 3.071 particles, $n = 35$ cells/embryos, $P < 0.0001$; comparison to *Cln1*$^{-/-}$ 1 μM NtBuHA = 2.711 particles, n = 28 cells/3 embryos, P < 0.0001, Šídák's multiple comparisons test (C) percent area of AFSM puncta per cell soma, *Cln1*$^{-/-}$ vehicle-treated = 2.062% of soma, n = 29 cells/3 embryos; comparison to *Cln1*$^{-/-}$ 10 μM NtBuHA = 0.8055% of soma, n = 25 cells/3 embryos, $P = 0.0012$; comparison to *Cln1*$^{-/-}$ 100 μM NtBuHA = 0.5546, n = 35 cells/3 embryos, $P = 0.0089$; comparison to *Cln1*$^{-/-}$ 1 mM NtBuHA = 0.8754, percent of soma, n = 28 cells/3 embryos, $P = 0.0095$, Šídák's multiple comparisons test. Data points on graphs represent values for individual cells.

percent of image area occupied by AFSM (Fig. 2C) were significantly diminished in NtBuHA-treated *Cln1*$^{-/-}$ mice at 2 months.

Next, we performed a long-term treatment paradigm, administering NtBuHA to *Cln1*$^{-/-}$ animals beginning at P30 and continuing to P180 (6 months of age). Informed by the preliminary results that 1 mM treatment had no adverse effects on the mice, together with toxicology data that the NOAEL (no observed adverse events level) of this compound is above 100 mg/kg, we increased the dosage to 4 mM (equivalent to 100 mg/kg). We then completed an identical histological analysis of 6-month (P180) old WT and *Cln1*$^{-/-}$ mice. While NtBuHA supplementation did not reduce AFSM puncta count at 6 months (Fig. 2B), it did diminish the percent area of AFSM in *Cln1*$^{-/-}$ mice (Fig. 2C).

In CLN1, progressive neuroinflammation can be characterized by increased numbers of glial fibrillary acidic protein (GFAP)-expressing astrocytes [36–38]. NtBuHA treatment (1 mM) has been shown to reduce GFAP-reactive cells in *Cln1*$^{-/-}$ mice at 6 months [26]. Building on these findings, we assessed the impact of chronic NtBuHA supplementation by quantifying GFAP-positive cells, and the area covered by GFAP immunolabeling in layer 2/3 of S1 and V1 in 2- and 6-month-old *Cln1*$^{-/-}$ mice (Fig. 2D-E, Supplemental Fig. 2). A significant elevation in astrogliosis was noted between 2 and 6 months in *Cln1*$^{-/-}$, aligning with disease progression (Fig. 2E). NtBuHA treatment significantly reduced astrogliosis both at 2 months (1 mM treatment) and 6 months (4 mM treatment), with decreased GFAP-positive cell counts (Fig. 2E) and reduced area occupied by GFAP+ cells (Supplementary Fig. 2C).

An additional indicator of neuroinflammation in CLN1 that intensifies with disease progression is microglial activation, detectable by the adoption of a pro-inflammatory morphology [39–41]. Morphological analysis of ionized calcium-binding adaptor molecule 1 (Iba1)-positive microglia in S1 and V1 revealed that *Cln1*$^{-/-}$ mice receiving NtBuHA exhibited an increased number of microglial process intersections and elongated average process length compared to untreated controls at both 2 and 6 months (Fig. 2F-G).

3.3. NtBuHA reduces synaptic calcium event frequency in *Cln1*$^{-/-}$ neurons

Recent studies from our lab demonstrated that *Cln1*$^{-/-}$ neurons exhibit aberrant postsynaptic calcium dynamics that underpin neuronal hyperexcitability in vitro and correspond to synchronous cortical neuron firing in vivo [29]. Therefore, we conducted a live cell imaging assay [28,29] in WT, *Cln1*$^{-/-}$, and NtBuHA-treated *Cln1*$^{-/-}$ primary cortical neurons to analyze the properties and dynamics of postsynaptic calcium influx at individual synapses (Fig. 3A, B). We first measured the amplitude of spontaneous calcium transients at dendritic boutons. Consistent with a previous report [28], spontaneous calcium transients were larger in *Cln1*$^{-/-}$ neurons than in WT cells, whereas NtBuHA-treated neurons demonstrated a surprising increase in calcium transient amplitude compared to untreated *Cln1*$^{-/-}$ neurons (Supplemental Fig. 3A). To test whether the amplitude of the most prominent synaptic calcium events in *Cln1*$^{-/-}$ neurons is affected by NtBuHA treatment, we considered the 200 highest amplitude calcium events from each group (Fig. 3C; Supplemental Fig. 3B). Using this metric, we again found that the largest spontaneous calcium transients were of greater amplitude in *Cln1*$^{-/-}$ neurons than in WT cells, while there was no difference between untreated and NtBuHA-treated *Cln1*$^{-/-}$ cells (Fig. 3C Supplemental Fig. 3B). Given this finding, we next considered the rate of spontaneous calcium events across each group. Here, we found that NtBuHA treatment had a marked effect on calcium event frequency. Specifically, while *Cln1*$^{-/-}$ neurons demonstrated a greater instantaneous event frequency compared to WT cells, exaggerated event frequency was normalized following NtBuHA treatment (Fig. 3D, E).

3.4. Impact of NtBuHA on seizure dynamics and motor function in *Cln1*−/− mice

Disease-modifying treatments for CLN1 Disease have historically generated mixed results on improving seizures in CLN1 mouse models [37,42]. We conducted EEG monitoring of epileptiform activity

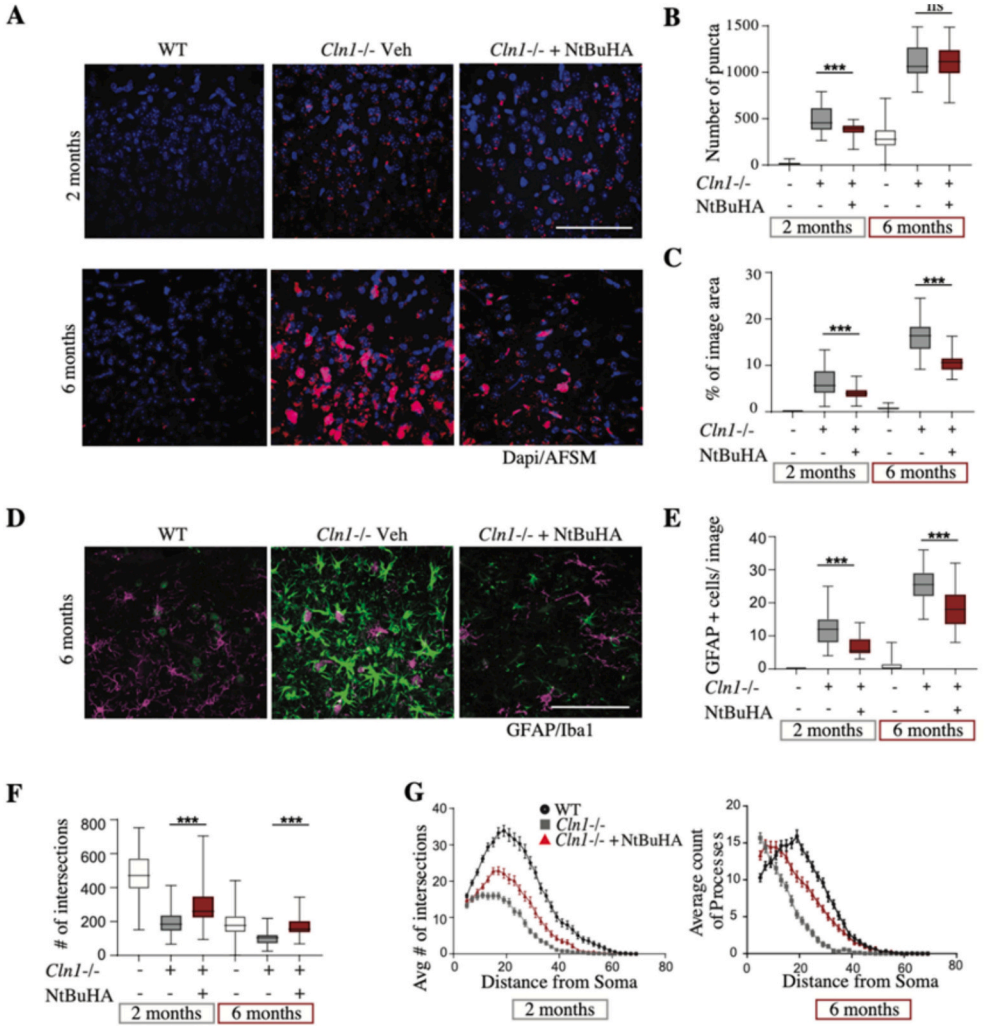

Fig. 2. Reduction of AFSM Accumulation and Neuroinflammation in *Cln1*$^{-/-}$ Mice Following NtBuHA Treatment. (A) Representative micrographs depicting AFSM accumulation in the visual cortex of Wild Type (WT), untreated *Cln1*$^{-/-}$, and *Cln1*$^{-/-}$ mice treated with 4 mM NtBuHA, at 6 months of age (P180), Scale = 100 μm. Quantification of (B) counts of AFSM puncta, 2 months: *Cln1*$^{-/-}$ = 500.2 particles, *n* = 30 images/ 3 mice; *Cln1*$^{-/-}$ 1 mM NtBuHA = 383.6 particles, *n* = 31 images/ 3 mice, *P* = 0.0018, Dunnett's multiple comparisons test. (C) the percentage of area covered by AFSM puncta in cortical sections, comparing WT, untreated *Cln1*$^{-/-}$, and NtBuHA-treated *Cln1*$^{-/-}$ mice at 2 and 6 months of age, 2 months: *Cln1*$^{-/-}$ = 6.409, n = 30 images/ 3 mice; *Cln1*$^{-/-}$ 1 mM NtBuHA = 3.933, n = 31 images/ 3 mice, *P* = 0.0013; Dunnett's multiple comparisons test; 6 months: *Cln1*$^{-/-}$ = 15.97, *n* = 39 images/ 3 mice; *Cln1*$^{-/-}$ 4 mM NtBuHA = 10.77, *n* = 43 images/ 3 mice, *P* < 0.0001, Tukey's multiple comparisons test. (D) Representative images GFAP (Green) and Iba1 (Magenta) immunostaining in the same 3 groups as (A) at 6 months of age. Scale = 100 μm. (E) Quantification of GFAP cell count per image in WT, *Cln1*$^{-/-}$, and NtBuHA-treated *Cln1*$^{-/-}$ cortex at 2 and 6 months of age, 2 months: *Cln1*$^{-/-}$ = 12.19 cells, n = 31 images/ 3 mice; *Cln1*$^{-/-}$ 1 mM NtBuHA = 4.567 cells, n = 31images/ 3 mice, P < 0.0001; 6 months: *Cln1*$^{-/-}$ = 25.53 cells, *n* = 34 images/ 3 mice; Cln1$^{-/-}$ 4 mM NtBuHA = 18.06 cells, *n* = 33 images/ 3 mice, *P* < 0.0001. (F) Quantification of total microglial arborizations. 2 months: *Cln1*$^{-/-}$ = 192.1 arborizations, *n* = 54 images/ 3 mice; *Cln1*$^{-/-}$ 1 mM NtBuHA = 292.4 arborizations, *n* = 52 images/ 3 mice, P < 0.0001. 6 months: *Cln1*$^{-/-}$ = 102.5 arborizations, *n* = 60 images/ 3 mice; *Cln1*$^{-/-}$ 4 mM NtBuHA = 167.8 arborizations, n = 60 images/ 3 mice, P < 0.0001. (G) Quantification of the number of arbors as a function of the distance from the cell soma using Scholl analysis WT, *Cln1*$^{-/-}$, and NtBuHA-treated *Cln1*$^{-/-}$ cortex at 2 months (left panel) and 6 months (right panel). Data are represented as mean ± SEM. Statistics for (E) and (F) were calculated using Tukey's multiple comparisons test. Data for B, C, E and F are in the format of box-and-whisker plots, indicating minimum to maximum values with a line representing the mean. (For interpretation of the references to colour in this figure legend, the reader is referred to the web version of this article.)

(represented by high amplitude spike trains) in WT and *Cln1*$^{-/-}$ animals treated long-term (from 1- to 7-months of age) with either NtBuHA (4 mM) or vehicle. For a subset of EEG recordings, time-stamped video recordings confirmed dynamic spike detection thresholding and were consistent with characteristic behavioral phenotypes of convulsant seizures recently reported in *Cln1*$^{-/-}$ mice (Supplemental Video 1–2) [42]. Crucially, treatment with NtBuHA diminished the number of spike trains (Fig. 4A; Supplemental Fig. 4), as well as the total and average spike train duration in *Cln1*$^{-/-}$ mice (Fig. 4B, C). Intriguingly, we found that NtBuHA-treated *Cln1*$^{-/-}$ mice had increased spike frequency, albeit this effect did not reach statistical significance (Fig. 3D). This seemingly paradoxical trend is consistent with human clinical studies showing diverse effects of anti-seizure medications on epileptic event propagation [11,12,43]. Our findings provide the first evidence for an effective treatment strategy that reduces seizures in *Cln1*$^{-/-}$ mice.

Finally, we assessed motor function using a fixed speed rotarod assay. Rotarod testing at 2 months of age showed no difference in the average latency to fall between WT, *Cln1*$^{-/-}$, and NtBuHA-treated *Cln1*$^{-/-}$ mice (Fig. 4E, *left*). At 4 and 6 months of age, untreated *Cln1*$^{-/-}$ animals demonstrated a significantly shorter latency to fall compared to WT counterparts. In contrast, *Cln1*$^{-/-}$ mice treated with NtBuHA (P30-P180) had no difference in latency to fall compared to WT (Fig. 4E, *middle and right*). Indeed, the behavioral performance of NtBuHA-treated *Cln1*$^{-/-}$ animals at 4 months approached, but did not

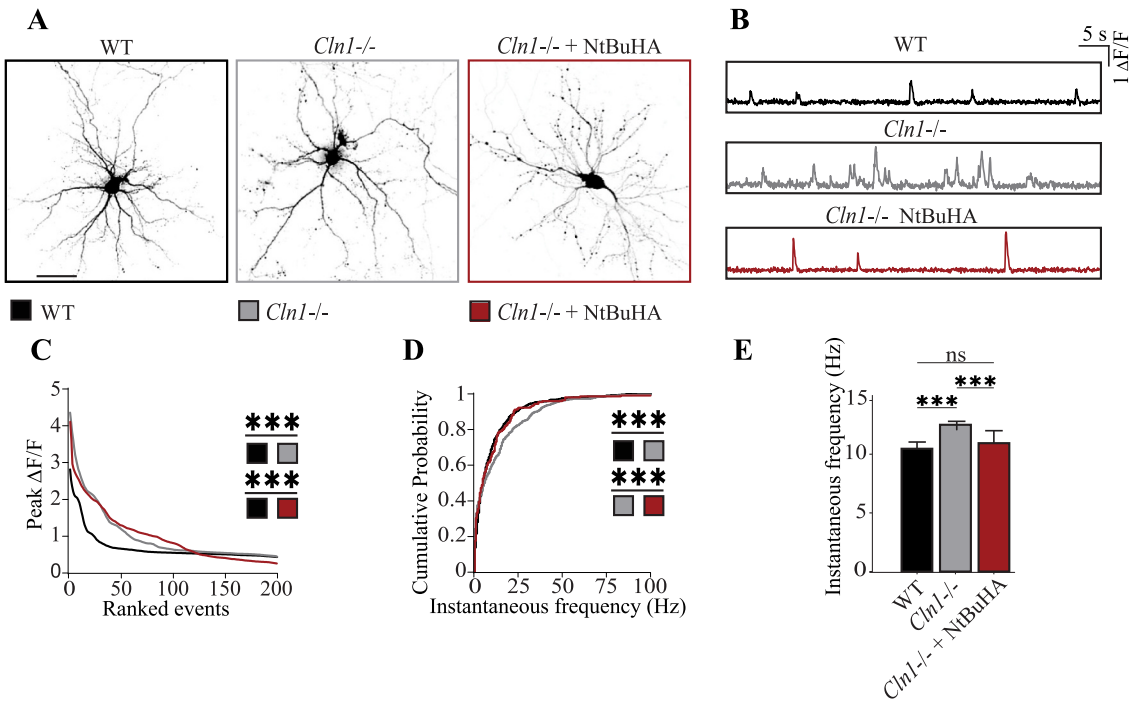

Fig. 3. Normalization of Synaptic Calcium Event Frequency via NtBuHA: (A) Example images of WT, *Cln1*$^{-/-}$, and NtBuHA-treated *Cln1*$^{-/-}$ neurons. Scale bar = 50 μm. (B) Example spontaneous calcium transients extracted from WT, *Cln1*$^{-/-}$, and NtBuHA-treated *Cln1*$^{-/-}$ neurons. (C) The amplitudes of the 200 largest events from each group are sorted in order. Mean amplitude values are as follows *Cln1*$^{-/-}$ = 0.92 ± 0.05, dF/F; WT = 0.60 ± 0.03 dF/F, *n* = 200 synaptic events; *P* < 0.001; WT = 0.60 ± 0.03 dF/F, n = 200 synaptic events; *Cln1*$^{-/-}$ + *NtBuHA* = 0.93 ± 0.05, dF/F, n = 200 synaptic events; *P* < 0.001. (D-E) Cumulative distributions of the instantaneous frequency of all detected calcium events from each group, *Cln1*$^{-/-}$ = 12.52 ± 0.65 Hz, *n* = 596 synaptic events; WT = 10.47 ± 0.52 Hz, *n* = 740 synaptic events; P < 0.001; *Cln1* $^{-/-}$ + NtBuHA = 10.95 ± 1.04 Hz, *n* = 191 synaptic events; P < 0.001, comparison to mutant untreated cells. Statistics for (C-E) were calculated using rank-sum tests. Live-cell imaging analysis was completed on a minimum of 3 genotyped embryos per group.

quite reach, a statistical improvement compared to untreated mice (Fig. 4E, *middle*).

4. Discussion

This study investigated the therapeutic effects of orally administered PPT1-mimetic small molecule, NtBuHA (CIRC827), in *Cln1*$^{-/-}$ mice. The results demonstrate that NtBuHA treatment decreased histological features of neuroinflammation, reduced AFSM accumulation, improved motor function, corrected synaptic calcium dynamics, and decreased the number and duration of seizures. These findings suggest a mechanism for how NtBuHA could be reducing seizure severity and indicate NtBuHA supplementation improves multiple layers of pathology in *Cln1*$^{-/-}$ mice.

4.1. Potential mechanisms for reduction of seizure with NtBuHA treatment

The global neuroinflammatory phenotype observed in *Cln1*$^{-/-}$ mice was robustly suppressed by NtBuHA treatment. While only 30 days of treatment (P30-P60) was sufficient to reduce gliosis, chronic treatment from one to six months blunted late-stage neuroinflammation as well. These data corroborate previous findings using NtBuHA, which demonstrate similar improvements to markers of neuroinflammation in four- and six-month old *Cln1*$^{-/-}$ mice [44]. Here, we provide additional evidence that microglial activation is also reduced by PPT1-mimetic treatment at six months [26]. While the presence of gliosis serves as a histopathological correlate of disease progression, it has also been causally implicated in several CLN1 disease processes, including the generation of seizures [45–47]. Further, microglial activation is associated with seizure onset in a CLN1 mouse model [40]. Therefore, one hypothesis is that NtBuHA treatment suppressed seizures via a reduction in neuroinflammation [40,42,44,48].

However, countervailing evidence for this interpretation comes from experiments employing chronic cannabidiol treatment in *Cln1*$^{-/-}$ mice [42], which suggest that neuroinflammatory severity and the emergence of seizures may be decoupled. That is, whereas cannabidiol supplementation successfully reduced microglial neuroinflammation, no parallel improvement in epileptic activity was observed [42]. While we suspect that diminishing neuroinflammation had a positive effect on seizure activity in NtBuHA-treated mice, the anti-seizure effects of the drug may also be driven by other mechanisms.

A growing body of evidence demonstrates that disrupted calcium dynamics in *Cln1*$^{-/-}$ neurons correlates with circuit-wide alterations to cortical neuron firing patterns [28,29]. Here, we demonstrate that chronic supplementation of NtBuHA in the medium of *Cln1*$^{-/-}$ primary cortical neurons corrected the increased frequency of postsynaptic calcium transients compared to untreated *Cln1*$^{-/-}$ neurons. Supporting this finding, recent work [48] shows that NtBuHA treatment impacts AMPA receptor transmission in hippocampal slices, although the effect was a reduction in the amplitude, rather than the frequency, of spontaneous postsynaptic events [48]. This discrepancy is reconciled by methodological differences. Namely, the study by Xia et al., used an acute (30 min) NtBuHA incubation and made physiological recordings of spontaneous postsynaptic events, which are AMPA receptor mediated, whereas we used a chronic treatment paradigm and imaged postsynaptic calcium transients, which involve both calcium permeable AMPA receptors and NMDA receptors [28,29]. These are crucial differences, considering Xia and colleagues noted a reduction in AMPA, but not NMDA receptor palmitoylation following acute NtBuHA treatment [48]; our previous data show that chronic palmitoylation inhibitor treatment can impact NMDA receptor palmitoylation [28]. Furthermore, we studied NtBuHA effects in *Cln1*$^{-/-}$ neurons, which demonstrate dysregulation of both glutamate receptor subtypes [28,29]. Taken together, it

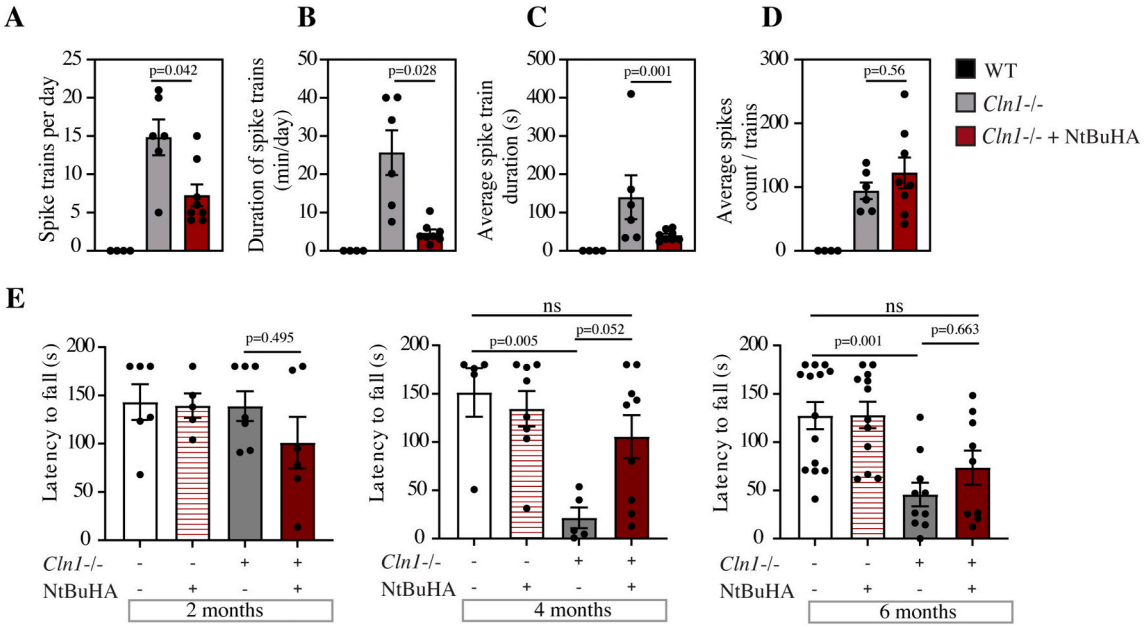

Fig. 4. Efficacy of NtBuHA in Modulating Seizure Activity and Motor Coordination in *Cln1*$^{-/-}$ Mice. Quantification of (A) total number of spike trains, *Cln1*$^{-/-}$ = 12.7 spikes, $n = 6$ mice; *Cln1*$^{-/-}$ 4 mM NtBuHA = 6.07 spikes, $n = 8$ mice, $P = 0.0072$. (B) Cumulative duration of spike trains, *Cln1*$^{-/-}$ = 23.95 min, n = 6 mice; *Cln1*$^{-/-}$ 4 mM NtBuHA = 3.739 min, n = 8 mice, $P = 0.0037$. (C) Average duration of spike trains, *Cln1*$^{-/-}$ = 140.2 min, n = 6 mice; *Cln1*$^{-/-}$ 4 mM NtBuHA = 40.06, n = 8 mice, $P = 0.001$, and (D) average spikes per train, compared across Wild Type (WT), *Cln1*$^{-/-}$, and NtBuHA-treated (4 mM) mice, using a spike detection threshold set at 5× baseline (Mann-Whitney test, *p*-values indicated), *Cln1*$^{-/-}$ = 94.15 spikes, n = 6 mice; *Cln1*$^{-/-}$ 4 mM NtBuHA = 122.3 spikes, n = 8 mice, $P = 0.5634$. (E) Rotarod performance tests at 2, 4, and 6 months of age for WT, NtBuHA-treated WT, *Cln1*$^{-/-}$, and NtBuHA-treated *Cln1*$^{-/-}$ mice ($n = 5$–9 mice/group); 2 months: WT = 143.1, seconds, n = 6 mice; *Cln1*$^{-/-}$ = 138.9, seconds, $n = 7$ mice, $P = 0.9985$, WT = 143.1, seconds, n = 6 mice; *Cln1*$^{-/-}$ 1 mM NtBuHA = 101.1, seconds, n = 6 mice, $P = 0.4368$, *Cln1*$^{-/-}$ = 138.9, seconds, n = 7 mice; *Cln1*$^{-/-}$ 1 mM NtBuHA = 101.1, seconds, n = 6 mice, $P = 0.4954$; 4 months: WT = 151.3, seconds, n = 5 mice; *Cln1*$^{-/-}$ = 21.46, seconds, n = 7 mice, $P = 0.0055$, WT = 151.3, seconds, n = 5 mice; *Cln1*$^{-/-}$ 4 mM NtBuHA = 105.5, seconds, $n = 9$ mice, $P = 0.4572$; 6 months: WT = 127.3, seconds, $n = 15$ mice; *Cln1*$^{-/-}$ = 45.71, seconds, n = 9 mice, $P = 0.0012$, WT = 127.3, seconds, n = 15 mice; *Cln1*$^{-/-}$ 4 mM NtBuHA = 73.51, n = 9 mice, $P = 0.06$. Statistics were all calculated using Tukey's multiple comparisons test unless otherwise specified.

appears that NtBuHA treatment duration selectively modulates glutamate receptor subtypes and their trafficking. Whereas acute treatment influences the short-term trafficking of AMPA receptors, chronic treatment likely affects both AMPA and NMDA receptor dynamics.

A holistic view of the evidence indicates that NtBuHA modulates synaptic activity and calcium entry through glutamate receptors. As abnormal neuronal calcium dynamics are implicated in epileptogenesis [49–51], this finding highlights the intriguing possibility that NtBuHA supplementation in *Cln1*$^{-/-}$ mice suppressed seizures through correcting synaptic calcium dynamics [51–53]. However, more experiments are required to determine whether the NtBuHA-mediated correction of synaptic transient frequency in vitro can be extrapolated to intact animals and whether such an effect is responsible for the alleviation of seizures observed in treated *Cln1*$^{-/-}$ mice. The reduction of seizure event frequency and duration in *Cln1*$^{-/-}$ mice is clinically significant, motivating further understanding of the potentially broad mechanism of action of NtBuHA.

4.2. Current therapeutic landscape for CLN1 and the translational potential of NtBuHA

The current clinical standard for CLN1 treatment is palliative care, as there are no approved treatment options that target the underlying cause of disease. The long-term goal is therefore to approve NtBuHA for use in CLN1 and provide clinicians the option of incorporating an orally administered, disease-treating small molecule into a patient's treatment plan.

Beyond the advances of NtBuHA as a small molecule-based treatment option for CLN1, significant advances have also been made in the development of both gene therapies and enzyme replacement therapies (ERTs). Viral-mediated gene therapies have shown promise for the treatment of CLN1 across several studies and treatment paradigms [20–22,52,53], and several important recent advancements in viral vector technology are working toward realizing the safe systemic delivery of a blood-brain barrier (BBB)-penetrant virus to achieve robust, widespread transduction of CNS cell-types [55,56]. Further, ERT has proven effective in *Cln1*$^{-/-}$ mice [37,57,58], with the most promising results coming from studies utilizing intracerebroventricular or intrathecal administration that allows intact enzyme to bypass the BBB [37,58]. However, the clinical application of both gene therapy and ERT approaches remains limited by a need to optimize the delivery (i.e., achieve widespread expression of the functional enzyme) and suppress potential adverse events [54].

Therefore, small molecule-based therapeutic strategies, either in isolation or in combination with gene therapy or ERT approaches, may offer a strategic benefit to treating CLN1. Many small molecules, such as NtBuHA, have good oral bioavailability and can cross the BBB. In addition to the practical benefits of oral administration, systemic delivery via this route allows for widespread distribution of drug to impact both the CNS and peripheral tissues. This feature may become increasingly important considering the growing evidence that CLN1 Batten Disease affects the spinal cord and enteric nervous system [55,56]. Further, with brain penetrant small molecules, distribution of the compound throughout the brain may supplement regions that may be more difficult to reach through the intrathecal or intraventricular injections often employed in ERTs [26,57].

There is an unmet need for a safe and effective curative therapy for CLN1 disease. A recent impactful study [37] demonstrating the efficacy of ERT in multiple animal models is promising. Here, we provide evidence for an additional near-term candidate for treating CLN1. Ongoing work includes further characterization of the dose-dependent pharmacodynamic and pharmacokinetic behavior of NtBuHA, as well as a Good

Laboratory Practices (GLP)-grade toxicology and safety pharmacology program in preparation for a First-in-Human trial. Specifically, Circumvent Pharmaceuticals is preparing toxicology and safety pharmacology studies required for an IND submission (in the US) and a CTA submission (in the EU). Clear next steps are to evaluate this formulation of NtBuHA (CIRC827) in a larger preclinical context, including larger animal models [24,37], in addition to testing its efficacy in combination with gene therapy and/or ERT approaches.

4.3. Therapeutic potential for NtBuHA beyond CLN1

We demonstrate herein that NtBuHA has manifold effects on neuronal and glial function in vivo. While an immediate goal is to optimize and employ NtBuHA to alleviate the suffering of CLN1 patients, our findings also point to a broader therapeutic potential for this small molecule. Firstly, lysosomal disruption is a characteristic of most common neurodegenerative diseases [57,58] including Alzheimer's disease [59], and NtBuHA reproducibly decreases lysosomal waste accumulation and improves lysosomal function [26,60]. Similarly, neuroinflammation is a common feature of many neurological conditions that is alleviated by NtBuHA treatment [61].

Also, while protein palmitoylation and depalmitoylation must be balanced for proper cellular function, this is particularly true for neurons. Synaptic proteins are significantly enriched for palmitoylation sites compared to the broader proteome [62], suggesting an outsized requirement for regulation of protein palmitoylation in the brain. It follows that dysregulated protein palmitoylation is associated with several neurological conditions, like Alzheimer's disease, where palmitoylation of the enzymes that process amyloid precursor protein affect disease progression [63]. This presents the intriguing possibility that therapeutics targeting protein palmitoylation will have particularly strong effects in the CNS, where existing treatments have a very high failure rate.

Finally, the aging brain demonstrates a generalized increase in protein palmitoylation that is associated with cognitive decline [64]. In this context (as well as those raised above), the broad depalmitoylase-mimetic activity and widespread distribution of small molecules such as NtBuHA may be leveraged to treat not only diseases caused by depalmitoylase mutation (i.e., CLN1), but a broader range of conditions associated with perturbations of protein palmitoylation. Taken together, NtBuHA targets several shared features of common neurological and neurodegenerative diseases, suggesting a broad therapeutic potential for NtBuHA beyond CLN1.

Supplementary data to this article can be found online at https://doi.org/10.1016/j.ymgme.2024.108537.

Funding

This research was funded in part by SBIR NS120360 and STTR HD105560 grants from the National Institute, as well as support from the NIH grant K99/R00 DC017754 to JDZ.

CRediT authorship contribution statement

Zach Fyke: Writing – review & editing, Writing – original draft, Visualization, Investigation, Formal analysis, Data curation, Conceptualization. **Rachel Johansson:** Writing – review & editing, Writing – original draft. **Anna I. Scott:** Writing – review & editing, Writing – original draft, Funding acquisition. **Devin Wiley:** Writing – review & editing, Writing – original draft, Funding acquisition, Conceptualization. **Daniel Chelsky:** Writing – review & editing, Writing – original draft, Project administration, Funding acquisition, Conceptualization. **Joseph D. Zak:** Writing – review & editing, Writing – original draft, Formal analysis. **Nader Al Nakouzi:** Writing – review & editing, Writing – original draft, Visualization, Project administration, Conceptualization. **Kevin P. Koster:** Writing – review & editing, Writing – original draft, Supervision, Conceptualization. **Akira Yoshii:** Supervision, Project administration, Funding acquisition, Conceptualization.

Declaration of competing interest

AIS and DW have stock in Circumvent. NAN, CH, PR and RJ all receive compensation for their time and expertise from Circumvent.

Data availability

Data will be made available on request.

Acknowledgments

The authors would like to thank Kamal Sharma and Lisa Hoffman for providing EEG recording hardware and training. We would also like to thank various past Yoshii lab members for helpful conversations and support. Additionally, this project is dedicated to Akira Yoshii, who sadly lost his battle with cancer during the course of this project. As a true physician-scientist, Akira's goal was to bridge the gap between bench & bedside. He hoped to accomplish this feat by conducting translational research in his lab, then administering effective treatments to children suffering from pediatric neurological diseases. We hope this study, along with others published posthumously, will in part fulfil his life's purpose.

References

[1] J. Vesa, E. Hellsten, L.A. Verkruyse, L.A. Camp, J. Rapola, P. Santavuori, S. L. Hofmann, L. Peltonen, Mutations in the palmitoyl protein thioesterase gene causing infantile neuronal ceroid lipofuscinosis, Nature 376 (1995) 584–587, https://doi.org/10.1038/376584a0.
[2] R.E. Williams, S.E. Mole, New nomenclature and classification scheme for the neuronal ceroid lipofuscinoses, Neurology 79 (2012) 183–191, https://doi.org/10.1212/wnl.0b013e31825f0547.
[3] D.A. Nita, S.E. Mole, B.A. Minassian, Neuronal ceroid lipofuscinoses, Epileptic Disord. 18 (2016), https://doi.org/10.1684/epd.2016.0844.
[4] M. Haltia, The neuronal ceroid-Lipofuscinoses, J. Neuropathol. Exp. Neurol. 62 (2003) 1–13, https://doi.org/10.1093/jnen/62.1.1.
[5] M. Haltia, The neuronal ceroid-lipofuscinoses: from past to present, Biochim. Biophys. Acta 1762 (2006) 850–856, https://doi.org/10.1016/j.bbadis.2006.06.010.
[6] A. Jalanko, T. Braulke, Neuronal ceroid lipofuscinoses, Biochim. Biophys. Acta 1793 (2009) 697–709, https://doi.org/10.1016/j.bbamcr.2008.11.004.
[7] G.W. Anderson, H.H. Goebel, A. Simonati, Human pathology in NCL, Biochim. Et Biophys. Acta Bba - Mol Basis Dis 2013 (1832) 1807–1826, https://doi.org/10.1016/j.bbadis.2012.11.014.
[8] E.F. Augustine, H.R. Adams, E. de los Reyes, K. Drago, M. Frazier, N. Guelbert, M. Laine, T. Levin, J.W. Mink, M. Nickel, D. Peifer, A. Schulz, A. Simonati, M. Topcu, J.A. Turunen, R. Williams, E.C. Wirrell, S. King, Management of CLN1 Disease: International Clinical Consensus, Pediatr. Neurol. 120 (2021) 38–51, https://doi.org/10.1016/j.pediatrneurol.2021.04.002.
[9] M. Nickel, C. Schwering, L. Westermann, E. Wibbeler, S. Lezius, A. Schulz, Hamburg iNCL scale: a new tool for the quantitative description of disease progression in infantile CLN1 patients, Neuropediatrics 52 (2021) S1–S53, https://doi.org/10.1055/s-0041-1739638.
[10] J. Radke, W. Stenzel, H.H. Goebel, Human NCL neuropathology, Biochim. Et Biophys. Acta Bba - Mol Basis Dis 2015 (1852) 2262–2266, https://doi.org/10.1016/j.bbadis.2015.05.007.
[11] N.H. Varvel, J. Jiang, R. Dingledine, Candidate drug targets for prevention or modification of epilepsy, Annu. Rev. Pharmacol. Toxicol. 55 (2015) 1–19, https://doi.org/10.1146/annurev-pharmtox-010814-124607.
[12] Y. Fukata, M. Fukata, Protein palmitoylation in neuronal development and synaptic plasticity, Nat. Rev. Neurosci. 11 (2010), https://doi.org/10.1038/nrn2788.
[13] P. Washbourne, Greasing transmission Palmitoylation at the synapse, Neuron 44 (2004) 901–902, https://doi.org/10.1016/j.neuron.2004.12.010.
[14] K.P. Koster, A. Yoshii, Depalmitoylation by Palmitoyl-protein Thioesterase 1 in neuronal health and degeneration, Front. Synapt. Neurosci. 11 (2019) 25, https://doi.org/10.3389/fnsyn.2019.00025.
[15] Y. Ohno, A. Kihara, T. Sano, Y. Igarashi, Intracellular localization and tissue-specific distribution of human and yeast DHHC cysteine-rich domain-containing proteins, Biochim. Biophys. Acta 1761 (2006) 474–483, https://doi.org/10.1016/j.bbalip.2006.03.010.
[16] R. Stix, C.-J. Lee, J.D. Faraldo-Gómez, A. Banerjee, Structure and mechanism of DHHC protein acyltransferases, J. Mol. Biol. 432 (2020) 4983–4998, https://doi.org/10.1016/j.jmb.2020.05.023.

[17] J.-Y.Y. Lu, S.L. Hofmann, Thematic review series: lipid posttranslational modifications. Lysosomal metabolism of lipid-modified proteins, J. Lipid Res. 47 (2006), https://doi.org/10.1194/jlr.r600010-jlr200.
[18] S.J. Won, M.C.S. Kit, B.R. Martin, Protein depalmitoylases, Crit. Rev. Biochem. Mol. Biol. 53 (2018) 83–98, https://doi.org/10.1080/10409238.2017.1409191.
[19] A. Schulz, T. Ajayi, N. Specchio, E.L. de Reyes, P. Gissen, D. Ballon, J.P. Dyke, H. Cahan, P. Slasor, D. Jacoby, A. Kohlschütter, C.S. Group, Study of intraventricular Cerliponase alfa for CLN2 disease, New Engl. J. Med. 378 (2018) 1898–1907, https://doi.org/10.1056/nejmoa1712649.
[20] M. Griffey, E. Bible, C. Vogler, B. Levy, P. Gupta, J. Cooper, M.S. Sands, Adeno-associated virus 2-mediated gene therapy decreases autofluorescent storage material and increases brain mass in a murine model of infantile neuronal ceroid lipofuscinosis, Neurobiol. Dis. 16 (2004) 360–369, https://doi.org/10.1016/j.nbd.2004.03.005.
[21] M.A. Griffey, D. Wozniak, M. Wong, E. Bible, K. Johnson, S.M. Rothman, A. E. Wentz, J.D. Cooper, M.S. Sands, CNS-directed AAV2-mediated gene therapy ameliorates functional deficits in a murine model of infantile neuronal ceroid lipofuscinosis, Mol. Ther. 13 (2006) 538–547, https://doi.org/10.1016/j.ymthe.2005.11.008.
[22] S.L. Macauley, M.S. Roberts, A.M. Wong, F. McSloy, A.S. Reddy, J.D. Cooper, M. S. Sands, Synergistic effects of central nervous system-directed gene therapy and bone marrow transplantation in the murine model of infantile neuronal ceroid lipofuscinosis, Ann. Neurol. 71 (2012) 797–804, https://doi.org/10.1002/ana.23545.
[23] B.E. Deverman, B.M. Ravina, K.S. Bankiewicz, S.M. Paul, D.W.Y. Sah, Gene therapy for neurological disorders: progress and prospects, Nat. Rev. Drug Discov. 17 (2018) 641–659, https://doi.org/10.1038/nrd.2018.110.
[24] S.L. Eaton, C. Proudfoot, S.G. Lillico, P. Skehel, R.A. Kline, K. Hamer, N. M. Rzechorzek, E. Clutton, R. Gregson, T. King, C.A. O'Neill, J.D. Cooper, G. Thompson, C.B. Whitelaw, T.M. Wishart, CRISPR/Cas9 mediated generation of an ovine model for infantile neuronal ceroid lipofuscinosis (CLN1 disease), Sci. Rep-Uk 9 (2019) 9891, https://doi.org/10.1038/s41598-019-45859-9.
[25] A. Shahryari, I. Burtscher, Z. Nazari, H. Lickert, Engineering gene therapy: advances and barriers, Adv. Ther. 4 (2021), https://doi.org/10.1002/adtp.202100040.
[26] C. Sarkar, G. Chandra, S. Peng, Z. Zhang, A. Liu, A.B. Mukherjee, Neuroprotection and lifespan extension in Ppt1−/− mice by NtBuHA: therapeutic implications for INCL, Nat. Neurosci. 16 (2013) 1608–1617, https://doi.org/10.1038/nn.3526.
[27] P. Gupta, A. Soyombo, A. Atashband, K. Wisniewski, J. Shelton, J. Richardson, R. Hammer, S. Hofmann, Disruption of PPT1 or PPT2 causes neuronal ceroid lipofuscinosis in knockout mice, in: Proceedings of the National Academy of Sciences 98, 2001, https://doi.org/10.1073/pnas.251485198.
[28] K.P. Koster, W. Francesconi, F. Berton, S. Alahmadi, R. Srinivas, A. Yoshii, Developmental NMDA receptor dysregulation in the infantile neuronal ceroid lipofuscinosis mouse model, Elife 8 (2019) e40316, https://doi.org/10.7554/elife.40316.
[29] K.P. Koster, E. Flores-Barrera, E.A. de la Villarmois, A. Caballero, K.Y. Tseng, A. Yoshii, Loss of Depalmitoylation disrupts homeostatic plasticity of AMPARs in a mouse model of infantile neuronal ceroid Lipofuscinosis, J. Neurosci. (2023), https://doi.org/10.1523/jneurosci.1113-23.2023. JN-RM-1113-23.
[30] E.A. Pnevmatikakis, A. Giovannucci, NoRMCorre: an online algorithm for piecewise rigid motion correction of calcium imaging data, J. Neurosci. Methods 291 (2017) 83–94, https://doi.org/10.1016/j.jneumeth.2017.07.031.
[31] A. Giovannucci, J. Friedrich, P. Gunn, J. Kalfon, B.L. Brown, S.A. Koay, J. Taxidis, F. Najafi, J.L. Gauthier, P. Zhou, B.S. Khakh, D.W. Tank, D.B. Chklovskii, E. A. Pnevmatikakis, CaImAn an open source tool for scalable calcium imaging data analysis, Elife 8 (2019) e38173, https://doi.org/10.7554/elife.38173.
[32] J.D. Zak, N.E. Schoppa, Neurotransmitter regulation rather than cell-intrinsic properties shapes the high-pass filtering properties of olfactory bulb glomeruli, J. Physiol. 600 (2022) 393–417, https://doi.org/10.1113/jp282374.
[33] J.D. Zak, G. Reddy, V. Konanur, V.N. Murthy, Distinct information conveyed to the olfactory bulb by feedforward input from the nose and feedback from the cortex, Nat. Commun. 15 (2024) 3268, https://doi.org/10.1038/s41467-024-47366-6.
[34] J.J. Kyle, S. Sharma, G. Tiarks, S. Rodriguez, A.G. Bassuk, Fast detection and quantification of Interictal spikes and seizures in a rodent model of epilepsy using an automated algorithm, Bio-Protoc. 13 (2023) e4632, https://doi.org/10.21769/bioprotoc.4632.
[35] A. Lundt, C. Wormuth, M.E. Siwek, R. Müller, D. Ehninger, C. Henseler, K. Broich, A. Papazoglou, M. Weiergräber, EEG Radiotelemetry in small laboratory rodents: a powerful state-of-the art approach in neuropsychiatric, Neurodegenerat. Epilepsy Res. Neural. Plast 2016 (2016) 8213878, https://doi.org/10.1155/2016/8213878.
[36] C. Kielar, L. Maddox, E. Bible, C.C. Pontikis, S.L. Macauley, M.A. Griffey, M. Wong, M.S. Sands, J.D. Cooper, Successive neuron loss in the thalamus and cortex in a mouse model of infantile neuronal ceroid lipofuscinosis, Neurobiol. Dis. 25 (2007) 150–162, https://doi.org/10.1016/j.nbd.2006.09.001.
[37] H.R. Nelvagal, S.L. Eaton, S.H. Wang, E.M. Eultgen, K. Takahashi, S.Q. Le, R. Nesbitt, J.T. Dearborn, N. Siano, A.C. Puhl, P.I. Dickson, G. Thompson, F. Murdoch, P.M. Brennan, M. Gray, S.N. Greenhalgh, P. Tennant, R. Gregson, E. Clutton, J. Nixon, C. Proudfoot, S. Guido, S.G. Lillico, C.B.A. Whitelaw, J.-Y. Lu, S.L. Hofmann, S. Ekins, M.S. Sands, T.M. Wishart, J.D. Cooper, Cross-species efficacy of enzyme replacement therapy for CLN1 disease in mice and sheep, J. Clin. Invest. 132 (2022) e163107, https://doi.org/10.1172/jci163107.
[38] S.L. Macauley, D.F. Wozniak, C. Kielar, Y. Tan, J.D. Cooper, M.S. Sands, Cerebellar pathology and motor deficits in the palmitoyl protein thioesterase 1-deficient mouse, Exp. Neurol. 217 (2009) 124–135, https://doi.org/10.1016/j.expneurol.2009.01.022.
[39] J.C. Savage, M. Carrier, M.-È. Tremblay, Morphology of microglia across contexts of health and disease, Meth. Mol. Biol. (Clifton, NJ) 2034 (2019) 13–26, https://doi.org/10.1007/978-1-4939-9658-2_2.
[40] X. Zhang, M. Wang, B. Feng, Q. Zhang, J. Tong, M. Wang, C. Lu, S. Peng, Seizures in PPT1 Knock-in mice are associated with inflammatory activation of microglia, Int. J. Mol. Sci. 23 (2022) 5586, https://doi.org/10.3390/ijms23105586.
[41] K. Berve, B.L. West, R. Martini, J. Groh, Sex- and region-biased depletion of microglia/macrophages attenuates CLN1 disease in mice, J. Neuroinflammation 17 (2020) 323, https://doi.org/10.1186/s12974-020-01996-x.
[42] J.T. Dearborn, H.R. Nelvagal, N.R. Rensing, K. Takahashi, S.M. Hughes, T. M. Wishart, J.D. Cooper, M. Wong, M.S. Sands, Effects of chronic cannabidiol in a mouse model of naturally occurring neuroinflammation, neurodegeneration, and spontaneous seizures, Sci. Rep-Uk 12 (2022) 11286, https://doi.org/10.1038/s41598-022-15134-5.
[43] M. Khateb, N. Bosak, M. Herskovitz, The effect of anti-seizure medications on the propagation of epileptic activity: a review, Front. Neurol. 12 (2021) 674182, https://doi.org/10.3389/fneur.2021.674182.
[44] T. Sadhukhan, M.B. Bagh, A.P. Appu, A. Mondal, W. Zhang, A. Liu, A.B. Mukherjee, In a mouse model of INCL reduced S-palmitoylation of cytosolic thioesterase APT1 contributes to microglia proliferation and neuroinflammation, J. Inherit. Metab. Dis. 44 (2021) 1051–1069, https://doi.org/10.1002/jimd.12379.
[45] D.C. Patel, B.P. Tewari, L. Chaunsali, H. Sontheimer, Neuron–glia interactions in the pathophysiology of epilepsy, Nat. Rev. Neurosci. 20 (2019) 282–297, https://doi.org/10.1038/s41583-019-0126-4.
[46] S. Robel, S.C. Buckingham, J.L. Boni, S.L. Campbell, N.C. Danbolt, T. Riedemann, B. Sutor, H. Sontheimer, Reactive Astrogliosis causes the development of spontaneous seizures, J. Neurosci. 35 (2015) 3330–3345, https://doi.org/10.1523/jneurosci.1574-14.2015.
[47] P.I. Ortinski, J. Dong, A. Mungenast, C. Yue, H. Takano, D.J. Watson, P.G. Haydon, D.A. Coulter, Selective induction of astrocytic gliosis generates deficits in neuronal inhibition, Nat. Neurosci. 13 (2010) 584–591, https://doi.org/10.1038/nn.2535.
[48] Z. Xia, Z. Shen, S. Zhang, J. Wang, T. Nie, Q. Deng, J. Chen, F. Wang, P. Wu, De-palmitoylation by N-(tert-butyl) hydroxylamine inhibits AMPAR-mediated synaptic transmission via affecting receptor distribution in postsynaptic densities, CNS Neurosci. Ther. 25 (2019) 187–199, https://doi.org/10.1111/cns.12996.
[49] R.J. DeLorenzo, D.A. Sun, L.S. Deshpande, Cellular mechanisms underlying acquired epilepsy: the calcium hypothesis of the induction and maintainance of epilepsy, Pharmacol. Ther. 105 (2005) 229–266, https://doi.org/10.1016/j.pharmthera.2004.10.004.
[50] S. Kovac, A.D. Kostova, A. Herrmann, N. Melzer, S. Meuth, A. Gorji, Metabolic and homeostatic changes in seizures and acquired epilepsy—mitochondria, calcium dynamics and reactive oxygen species, Int. J. Mol. Sci. 18 (2017) 1935, https://doi.org/10.3390/ijms18091935.
[51] M. Raza, R.E. Blair, S. Sombati, D.S. Carter, L.S. Deshpande, R.J. DeLorenzo, Evidence that injury-induced changes in hippocampal neuronal calcium dynamics during epileptogenesis cause acquired epilepsy, Proc. Natl. Acad. Sci. 101 (2004) 17522–17527, https://doi.org/10.1073/pnas.0408155101.
[52] S.L. Macauley, A.M.S. Wong, C. Shyng, D.P. Augner, J.T. Dearborn, Y. Pearse, M. S. Roberts, S.C. Fowler, J.D. Cooper, D.M. Watterson, M.S. Sands, An anti-Neuroinflammatory that targets dysregulated glia enhances the efficacy of CNS-directed gene therapy in murine infantile neuronal ceroid Lipofuscinosis, J. Neurosci. 34 (2014) 13077–13082, https://doi.org/10.1523/jneurosci.2518-14.2014.
[53] C. Shyng, H.R. Nelvagal, J.T. Dearborn, J. Tyynelä, R.E. Schmidt, M.S. Sands, J. D. Cooper, Synergistic effects of treating the spinal cord and brain in CLN1 disease, Proc. National Acad. Sci. 114 (2017) E5920–E5929, https://doi.org/10.1073/pnas.1701832114.
[54] A. Biffi, Gene therapy for lysosomal storage disorders: a good start, Hum. Mol. Genet. 25 (2016) R65–R75, https://doi.org/10.1093/hmg/ddv457.
[55] J.R. Ostergaard, H.R. Nelvagal, J.D. Cooper, Top-down and bottom-up propagation of disease in the neuronal ceroid lipofuscinoses, Front. Neurol. 13 (2022) 1061363, https://doi.org/10.3389/fneur.2022.1061363.
[56] C. Parker, J. Zhao, D.A. Pearce, A.D. Kovács, Comparative analysis of the gut microbiota composition in the Cln1R151X and Cln2R207X mouse models of batten disease and in three wild-type mouse strains, Arch. Microbiol. 203 (2021) 85–96, https://doi.org/10.1007/s00203-020-02007-6.
[57] V. Udayar, Y. Chen, E. Sidransky, R. Jagasia, Lysosomal dysfunction in neurodegeneration: emerging concepts and methods, Trends Neurosci. 45 (2022) 184–199, https://doi.org/10.1016/j.tins.2021.12.004.
[58] R.A. Nixon, The aging lysosome: an essential catalyst for late-onset neurodegenerative diseases, Biochim. Biophys. Acta (BBA) - Proteins Proteom. 1868 (2020) 140443, https://doi.org/10.1016/j.bbapap.2020.140443.
[59] R.A. Nixon, Amyloid precursor protein and endosomal-lysosomal dysfunction in Alzheimer's disease: inseparable partners in a multifactorial disease, FASEB J. 31 (2017) 2729–2743, https://doi.org/10.1096/fj.201700359.
[60] M.B. Bagh, S. Peng, G. Chandra, Z. Zhang, S.P. Singh, N. Pattabiraman, A. Liu, A. B. Mukherjee, Misrouting of v-ATPase subunit V0a1 dysregulates lysosomal acidification in a neurodegenerative lysosomal storage disease model, Nat. Commun. 8 (2017) 14612, https://doi.org/10.1038/ncomms14612.
[61] R.M. Ransohoff, How neuroinflammation contributes to neurodegeneration, Science 353 (2016) 777–783, https://doi.org/10.1126/science.aag2590.
[62] S.S. Sanders, D.D.O. Martin, S.L. Butland, M. Lavallée-Adam, D. Calzolari, C. Kay, J.R. Yates, M.R. Hayden, Curation of the mammalian Palmitoylome indicates a pivotal role for Palmitoylation in diseases and disorders of the nervous system and

cancers, PLoS Comput. Biol. 11 (2015) e1004405, https://doi.org/10.1371/journal.pcbi.1004405.

[63] R. Bhattacharyya, C. Barren, D.M. Kovacs, Palmitoylation of amyloid precursor protein regulates Amyloidogenic processing in lipid rafts, J. Neurosci. 33 (2013) 11169–11183, https://doi.org/10.1523/jneurosci.4704-12.2013.

[64] D.R. Zamzow, V. Elias, V.A. Acosta, E. Escobedo, K.R. Magnusson, Higher levels of protein Palmitoylation in the frontal cortex across aging were associated with reference memory and executive function declines, ENeuro 6 (2019), https://doi.org/10.1523/eneuro.0310-18.2019. ENEURO.0310-18.2019.